PAPER

Check for updates

Three dimensional Ni$_{1+x}$Fe$_{2-x}$S$_4$-graphene-2D-MoSe$_2$ as an efficient material for supercapacitors†

Xiao-Feng Tang, [ID] [a] Zhen-Guo Yang*[a] and Jia-Hui Liang[b]

A ternary Ni$_{1+x}$Fe$_{2-x}$S$_4$-graphene-2D-MoSe$_2$ (Ni$_{1+x}$Fe$_{2-x}$S$_4$-g-MoSe$_2$) nanocomposite was designed and fabricated through a facile two-step method. Well-dispersed Ni$_{1+x}$Fe$_{2-x}$S$_4$ nanoparticles on graphene sheets were achieved using a hydrothermal method followed by coating with MoSe$_2$ nanosheets using *in situ* adsorption. The synergistic effect of the three components present in Ni$_{1+x}$Fe$_{2-x}$S$_4$-g-MoSe$_2$ yielded enhanced electrochemical properties in terms of high specific capacitance reaching up to 2108 F g^{-1} at a current density of 1 A g^{-1}, with capacity retention of 93.3% after 4000 cycles at the high charge–discharge current density of 5 A g^{-1}. These outstanding capacitance features were mainly attributed to the unique Ni$_{1+x}$Fe$_{2-x}$S$_4$-g-MoSe$_2$ nanostructure, allowing easy access to the pseudocapacitive species and fast ion/electron transfer. Overall, the prepared 3D nanocomposite is promising as an electrode material for advanced supercapacitors.

1. Introduction

In the past few years, the increasing demand for large-scale industrial operations has created a new direction focusing on high power and energy-density storage devices.[1–6] Among them, supercapacitors (SCs) have attracted particular attention due to their large power densities, long cycle life (>100 000 cycles), and rapid charge–discharge rates.[7–12] It is widely accepted that the key to developing effective SCs relies on the design and synthesis of high-performance electrode materials.[13–16] Generally, SCs can be divided into two groups based on their energy storage mechanisms: (i) electrical double-layer capacitors (EDLCs) based on carbon-active materials as electrodes,[17–19] and (ii) pseudocapacitors consisting mainly of redox-active materials.[20–24]

To date, numerous carbonaceous materials, including activated carbon, mesoporous carbon, carbon nanotubes and graphene have been investigated for EDLC electrodes.[25–27] However, although carbon-based capacitors provide higher power densities, their energy densities are lower than those of pseudocapacitors. On the other hand, pseudocapacitors suffer from inferior cycling abilities while they possess much higher energy densities.[28–31] To reconcile the disadvantages of each SC type, one strategy is to combine both electrode materials by coupling pseudocapacitors with EDLCs based carbon materials.[27,32–35]

More recent research investigations have been focusing on ternary composites because of their enhanced electrochemical

performances when compared to binary composites.[26,36–38] The combination between properties of individual components often boosts the performance of the electrodes. However, unfortunately, the pseudocapacitive performance of the hybrid materials is still lacklustre. They lack well-defined nanostructures and inadequate synergistic effects. Thus, a pivotal challenge in energy storage devices is to construct integrated nanoarchitecture of hybrid materials with excellent synergistic effects, where the structural features and electroactivities of each constituent could fully manifest with rapid ion/electron transport.[39–45]

Two-dimensional (2D) materials, such as molybdenum selenide (MoSe$_2$), are considered as active components for energy devices because of their unique nanosheet morphology and large surface area.[46–48] However, using MoSe$_2$ only still suffer from poor electrochemical properties. A feasible way to overcome this issue is by combining MoSe$_2$ with conductive matrices, like graphene and pseudocapacitors to improve the specific capacitance and rate capability of the resulting electrodes. Despite the great efforts devoted in this field, the resulting MoSe$_2$ nanosheets still suffer from agglomerations and separation from the graphene sheets due to the poor interfacial properties. By contrast, ternary co-metal sulfide, such as NiCo$_2$S$_4$, could result in better SCs properties because of its rich redox reactions than binary nickel sulfide and cobalt sulfide.[29,31]

In this study, the design and fabrication of unique three-dimensional (3D) Ni$_{1+x}$Fe$_{2-x}$S$_4$-graphene-2D-MoSe$_2$ (Ni$_{1+x}$Fe$_{2-x}$S$_4$-g-MoSe$_2$) hybrid was performed through a two-step hydrothermal method followed by adsorption. The morphology, microstructure and electrochemical properties of the obtained Ni$_{1+x}$Fe$_{2-x}$S$_4$-g-MoSe$_2$ in comparison with separate components were investigated. The contributions of the different components in the electrochemical performances were also discussed.

*a*Department of Materials Science, Fudan University, Shanghai, 200433, P. R. China. E-mail: zgyang@fudan.edu.cn; Fax: +86-021-65642523; Tel: +86-021-65642523

*b*College of Materials Science and Engineering, Donghua University, Shanghai 201620, P. R. China

Compared to $Ni_{1+x}Fe_{2-x}S_4$-g and $Ni_{1+x}Fe_{2-x}S_4$-$MoSe_2$ counterparts, the fabricated $Ni_{1+x}Fe_{2-x}S_4$-g-$MoSe_2$ exhibited remarkable electrochemical performances with higher capacitance values and long cycle life.

2. Experimental

2.1 Materials and synthesis

Graphite and $MoSe_2$ (99.9%) were purchased from Sigma-Aldrich. All the other chemicals were of analytical grade and used as-received without further purification. Double distilled water was used for the preparation of the aqueous solutions and washing processes.

2.2 Preparation of $Ni_{1+x}Fe_{2-x}S_4$-g-$MoSe_2$ nanocomposite

The following procedure was used for the synthesis of the Ni_{1+x}-$Fe_{2-x}S_4$-g-$MoSe_2$ nanocomposite. Firstly, graphene and $MoSe_2$ nanosheets were prepared according to our previously published report using an initial concentration of 3 mg mL^{-1}.[49] Next, Ni $(NO_3)_2 \cdot 6H_2O$ (1 mmol), $FeCl_3 \cdot 6H_2O$ (2 mmol) and thiourea (9 mmol) were dissolved in 25 mL of graphene solution (IPA/water 1 : 1). Ammonia (1 mL) was then added dropwise to the solution followed by magnetic stirring for 0.5 h and sonication for 1 h. The mixture was transferred into a Teflon-lined autoclave, then sealed and heated at 200 °C in an oven for 24 h. The obtained product was filtered off and the collected solid was washed three times with water and ethanol and dried in a vacuum oven at 60 °C for 12 h to yield $Ni_{1+x}Fe_{2-x}S_4$-g, which was placed in 25 mL $MoSe_2$ nanosheet solution (IPA/water 1 : 1) under sonication for 30 min. Finally, the mixture was left to rest for 24 h, and the resulting $Ni_{1+x}Fe_{2-x}S_4$-g-$MoSe_2$ nanocomposite was filtered off and dried in a vacuum. For comparison, the $Ni_{1+x}Fe_{2-x}S_4$-$MoSe_2$ counterpart was obtained by the same procedure but without adding the graphene solution. The synthesis process is shown in Fig. 1.

The working electrodes were prepared by mixing 80 wt% active material, 10 wt% polyvinylidene fluoride (PVDF) and 10 wt% carbon black. The mixture was then dispersed in N-methyl-2-pyrrolidone to form a homogeneous slurry. After that, the slurry was pasted on nickel foams and pressed into thin disk electrodes with uniform thicknesses (10 MPa for 1 min). The mass loading of the active materials on each electrode was approximately 4 mg cm^{-2}.

2.3 Characterization

The X-ray diffraction (XRD) patterns were recorded on a Rigaku D/MaxUltima II Powder XRD 6s X-ray diffractometer, operating at 40 kV and 20 mA using Cu K radiation ($\lambda = 0.15406$ nm). Fourier transformation infrared profiles (FTIR) were measured on a Nicolet 670 spectrometer using KBr pellets. UV-Vis diffusive reflectance spectra were acquired on a Shimadzu UV-3600 spectrophotometer. Raman was conducted using a 514 nm wavelength laser on a RENISHAW invia Raman Microscope. Thermogravimetric analysis (TGA) was conducted on a TA Q-600 from ambient temperature to 600 °C in argon atmosphere at a heating rate of 10 °C min^{-1}. The elemental compositions were determined using XPS (PHI Quantera X-ray photoelectron spectrometer). The morphologies of the nanocomposites were obtained by field emission scanning electron microscopy (FEI Quanta 400 ESEM FEG), transmission electron microscopy (TEM), and high-resolution TEM (HRTEM) acquired with a JEOL 2010 at the acceleration voltage of 200 kV. Nitrogen adsorption–desorption isotherms were carried out on Micromeritics Tristar 3000 porosimeter at 77 K.

An Autolab 302 electrochemical workstation was used to characterize the electrochemical behaviors. A three-electrode glass cell containing 6 M KOH aqueous electrolyte was employed for the electrochemical measurements. The cyclic voltammetry (CV) curves were obtained at various scan rates (5, 10, 20, 50, and 100 mV s^{-1}) in the potential window of 0–0.6 V. The galvanostatic charge–discharge (GCD) was recorded at various current densities (1, 2, 5, 10 and 20 A g^{-1}) in the potential window of 0–0.4 V.
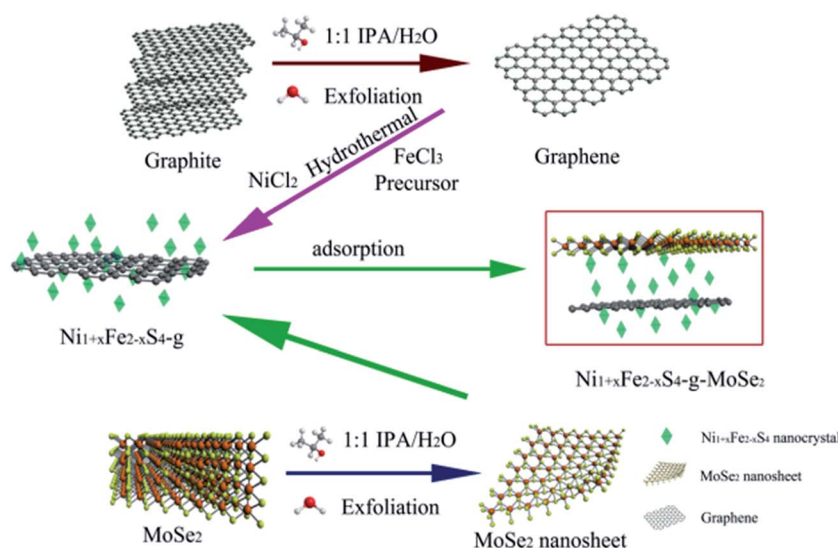

Fig. 1 The process used for the preparation of $Ni_{1+x}Fe_{2-x}S_4$-g-$MoSe_2$.

3. Results and discussion

3.1 Characterization

Fig. 2a shows the XRD patterns of the as-prepared samples. Except the few peaks indexed to $MoSe_2$, all the other features could be ascribed to the cubic phase of $Ni_{1+x}Fe_{2-x}S_4$ (JCPDS no. 47-1740). The shift of the (002) peak to lower 2θ values when compared to bulk $MoSe_2$ suggested an expanded layer space in $MoSe_2$, resulting from the liquid phase exfoliation (LPE).

Fig. 2b illustrates the TGA curves of $Ni_{1+x}Fe_{2-x}S_4$, $Ni_{1+x}Fe_{2-x}S_4$-g, $Ni_{1+x}Fe_{2-x}S_4$-$MoSe_2$, and $Ni_{1+x}Fe_{2-x}S_4$-g-$MoSe_2$. A weight loss of $Ni_{1+x}Fe_{2-x}S_4$ occurred in the 400–600 °C range (Fig. 2b), attributed to the thermal decomposition of $Ni_{1+x}Fe_{2-x}S_4$. The TGA profiles indicated that the addition of graphene and $MoSe_2$ nanosheets improved the thermal stability of the nanocomposites.

The Raman spectra of the samples are depicted in Fig. S1.† The spectra consisted of sharp peaks between 200 and 600 cm^{-1}, typically associated with the crystalline $Ni_{1+x}Fe_{2-x}S_4$ and $MoSe_2$. The peaks were overlapped with each other, making them hard to distinguish. D and G peaks of graphene were visible around 1300–1600 cm^{-1}.

The FTIR spectra of $Ni_{1+x}Fe_{2-x}S_4$, $Ni_{1+x}Fe_{2-x}S_4$-g, $Ni_{1+x}Fe_{2-x}S_4$-$MoSe_2$ and $Ni_{1+x}Fe_{2-x}S_4$-g-$MoSe_2$ are gathered in Fig. S2.† Typical peaks of $Ni_{1+x}Fe_{2-x}S_4$ and $MoSe_2$ can be seen around 600 and 1100 cm^{-1} while the characteristic skeletal vibration of C=C in graphene nanosheets appeared at 1625 cm^{-1}. This confirmed the formation of the sp^2 carbon skeleton.

To gain further information on the chemical state of $Ni_{1+x}Fe_{2-x}S_4$ in $Ni_{1+x}Fe_{2-x}S_4$-g-$MoSe_2$, X-ray photoelectron spectroscopy (XPS) was conducted and the results are shown in Fig. S3.†
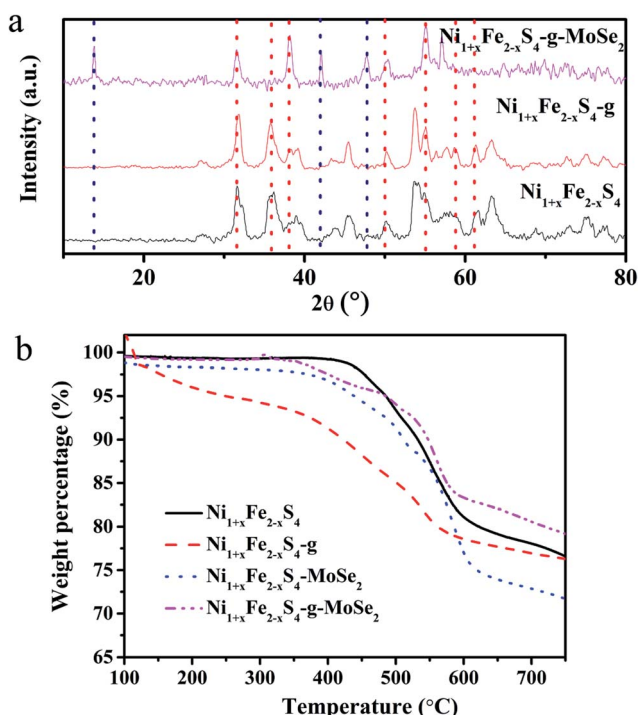
The XPS survey spectrum of $Ni_{1+x}Fe_{2-x}S_4$-g-$MoSe_2$ indicated the presence of C, Ni, Fe, Mo and Se elements (Fig. S3a†). As shown in Fig. S3b,† the binding energies of Fe $2p_{3/2}$ and Fe $2p_{1/2}$ were recorded at 711.4 and 724.9 eV, respectively. Similarly, the Ni 2p spectrum (Fig. S3c†) can be fitted by two spin–orbit doublets, characteristic of Ni^{2+} and Ni^{3+} with two shake-up satellites. The Mo 3d (Fig. S3d†) and Se 2p spectra (Fig. S3e†) can also be divided into two main peaks.

Overall, XRD, TGA, FTIR, Raman and XPS analysis showed that the ternary $Ni_{1+x}Fe_{2-x}S_4$-g-$MoSe_2$ nanocomposite and its counterparts were successfully prepared.

SEM and TEM were conducted to analyze the morphology of the samples. $Ni_{1+x}Fe_{2-x}S_4$-g-$MoSe_2$ exhibited typical clusters of nanosheets (Fig. 3a). The high magnification image shown in Fig. 3b revealed that $Ni_{1+x}Fe_{2-x}S_4$, graphene and $MoSe_2$ nanosheets were interconnected. The TEM of $Ni_{1+x}Fe_{2-x}S_4$-g-$MoSe_2$ further indicated that the $Ni_{1+x}Fe_{2-x}S_4$ sheets were composed of nanoparticles with average diameters of about 20 nm lying on graphene and $MoSe_2$ sheets (Fig. 3c). The microstructure of $Ni_{1+x}Fe_{2-x}S_4$-g-$MoSe_2$ was further investigated by HRTEM, and the data are illustrated in Fig. 3d. The lattice fringes could be assigned to the following crystal planes: 0.34 nm for graphene (002) and 0.28 nm for $MoSe_2$ (002). Moreover, from the electron diffraction pattern, it could be found that mixed pattern of crystals exist. The collected indices were consistent with the XRD data, demonstrating the successful formation of sheet-particle-sheet structure.

Based on the different characterizations, the formation of $Ni_{1+x}Fe_{2-x}S_4$-g-$MoSe_2$ could be explained by the following mechanism: before performing the hydrothermal process, IPA was first mixed with water to form a uniform co-solvent for LPE of graphite and $MoSe_2$. Polar solutes and water are known to be miscible at the thermodynamic equilibrium and tend to self-aggregate to form microemulsions. Thus, Fe^{3+} and Ni^{2+} were absorbed onto the micro-liquid drops during the hydrothermal process. The reaction of Fe^{3+} and Ni^{2+} with OH^{-1} assembled the species into nanoparticles. Next, the Ostwald-ripening of the

Fig. 2 XRD patterns (a) and TGA curves (b) of $Ni_{1+x}Fe_{2-x}S_4$, $Ni_{1+x}Fe_{2-x}S_4$-g, $Ni_{1+x}Fe_{2-x}S_4$-$MoSe_2$, and $Ni_{1+x}Fe_{2-x}S_4$-g-$MoSe_2$.
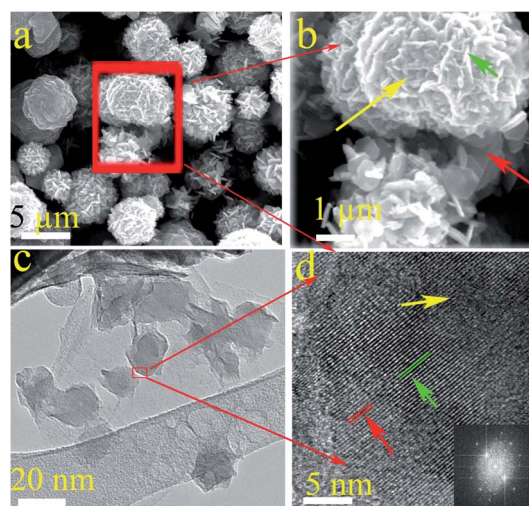

Fig. 3 Low and high-resolution SEM (a and b) and TEM images (c and d) of $Ni_{1+x}Fe_{2-x}S_4$-g-$MoSe2$. Inset is the corresponding electron diffraction pattern.
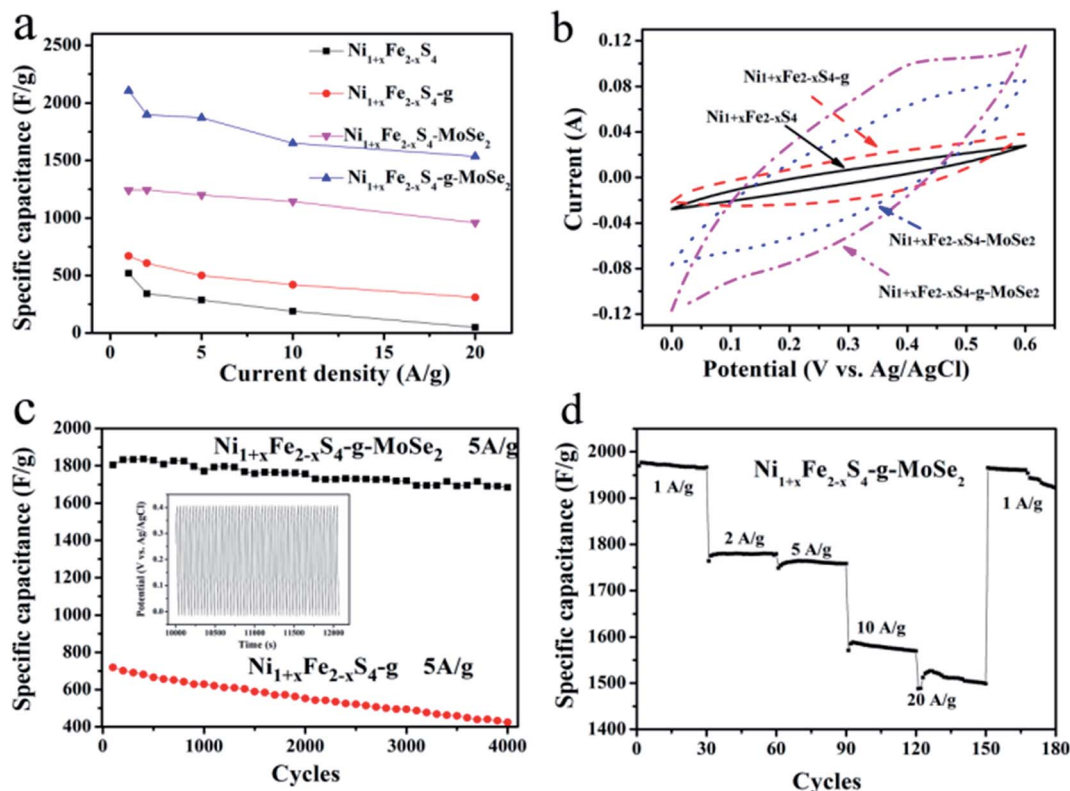
Fig. 4 (a) Specific capacitance of $Ni_{1+x}Fe_{2-x}S_4$, $Ni_{1+x}Fe_{2-x}S_4$-g, $Ni_{1+x}Fe_{2-x}S_4$-MoSe$_2$, and $Ni_{1+x}Fe_{2-x}S_4$-g-MoSe$_2$ at different current densities. (b) CV curves of $Ni_{1+x}Fe_{2-x}S_4$, $Ni_{1+x}Fe_{2-x}S_4$-g, $Ni_{1+x}Fe_{2-x}S_4$-MoSe$_2$ and $Ni_{1+x}Fe_{2-x}S_4$-g-MoSe$_2$ at a scan rate of 5 mV s^{-1}. (c) Comparison between $Ni_{1+x}Fe_{2-x}S_4$-g-MoSe$_2$ and $Ni_{1+x}Fe_{2-x}S_4$-g during long cycling. (d) Cycle stability of $Ni_{1+x}Fe_{2-x}S_4$-g-MoSe$_2$ at different current densities (d).

assembled microspheres aggregated the $Ni_{1+x}Fe_{2-x}S_4$ nanoparticles into nanosheets, and recrystallization occurred on both the outside and inside of the microspheres during the gradual sulfuration process with S^{2-}.

4. Electrochemical performance

The electrochemical performances of all samples were investigated by galvanostatic charge–discharge (GCD) and CV measurements in 6 M KOH as the electrolyte. The GCD curves were measured in the potential window of 0–0.4 V, and the data are shown in Fig. 4a and S4.† The specific capacitance was calculated according to eqn (1).

$$C_m = \frac{I\Delta t}{m\Delta V} \left(\text{F g}^{-1}\right) \tag{1}$$

where C is specific capacitance (F g^{-1}), I is the charge–discharge current (A), m is the mass of the active material present on one electrode (g), ΔV is the potential window, and Δt is the discharge time (s).

Fig. 4a summarizes the calculated responses of $Ni_{1+x}Fe_{2-x}S_4$, $Ni_{1+x}Fe_{2-x}S_4$-g, $Ni_{1+x}Fe_{2-x}S_4$-MoSe$_2$ and $Ni_{1+x}Fe_{2-x}S_4$-g-MoSe$_2$ at different current densities ranging from 1 to 20 A g^{-1}. Apparently, the addition of graphene and MoSe$_2$ nanosheets enhanced the SC composed of ternary composite-a product due to the effective electrochemical utilization of $Ni_{1+x}Fe_{2-x}S_4$. The $Ni_{1+x}Fe_{2-x}S_4$-g-MoSe$_2$ composite exhibited excellent capacitance reaching up to

2108, 1898, 1872, 1650 and 1536 F g^{-1} at current densities of 1, 2, 5, 10 and 20 A g^{-1}, respectively. These values were much higher than those obtained with the $Ni_{1+x}Fe_{2-x}S_4$-based counterparts.
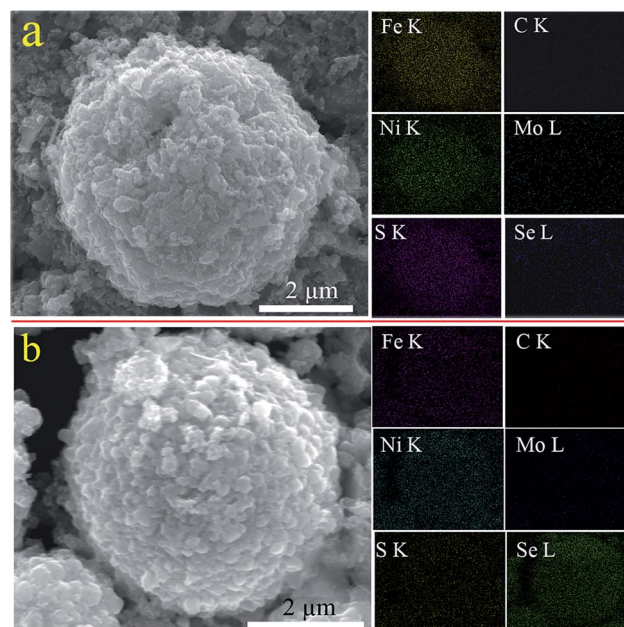

Fig. 5 SEM and EDX mapping of $Ni_{1+x}Fe_{2-x}S_4$-g-MoSe$_2$ before (a) and after (b) cycling.

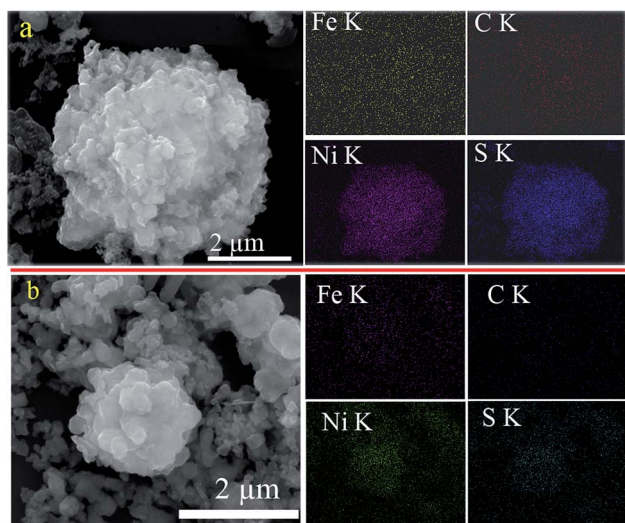**Fig. 6** SEM and EDX mapping of $Ni_{1+x}Fe_{2-x}S_4$-g before (a) and after (b) cycling.

As shown in the CV of Fig. 4b and S5,† the area surrounded by the CV curve of $Ni_{1+x}Fe_{2-x}S_4$-g-MoSe$_2$ in the three-electrode systems was the largest, meaning a highest capacitance when compared to other $Ni_{1+x}Fe_{2-x}S_4$-containing samples. The material amount and device capacitance (C_m, F g^{-1}) can be calculated using the CV measurements and eqn (2).

$$C_m = \frac{\int I(V)dv}{vm\Delta V} \left(F\ g^{-1} \right) \qquad (2)$$

where m is the total mass of the electroactive material in both the positive and negative electrodes (g), v is the scan rate (V s^{-1}), and ΔV is the potential window (V). As the scan rate increased, the anodic peak shifted slightly towards the positive potential, which is probably originated from the $Ni_{1+x}Fe_{2-x}S_4$-g-MoSe$_2$ nanocomposite electrode.

Long cycle life is another imperative criterion of commercial SCs. To confirm the advantages of the ternary composite in the effective electrochemical utilization of $Ni_{1+x}Fe_{2-x}$ and MoSe$_2$, long cycle charge–discharge testing was conducted for

$Ni_{1+x}Fe_{2-x}$-g and $Ni_{1+x}Fe_{2-x}$-g-MoSe$_2$, and the results are shown in Fig. 4c. Compared to $Ni_{1+x}Fe_{2-x}$-g, the $Ni_{1+x}Fe_{2-x}$-g-MoSe$_2$ composite exhibited far higher specific capacitance and cycling stability values. The specific capacitance initially increased due to the full activation of $Ni_{1+x}Fe_{2-x}S_4$, with no obvious degradation of the active material after 4000 cycles retaining 93.3% of the initial capacity. Fig. 4d illustrated that bringing the current density to 1 A g^{-1} after one whole cycle induced no significant change in the specific capacitance. This further confirmed the excellent electrochemical stability and rate capability of Ni_{1+x}-Fe$_{2-x}$S$_4$-g-MoSe$_2$.

To gain a better understanding of the long-life performance of $Ni_{1+x}Fe_{2-x}S_4$-g-MoSe$_2$, the material was extracted from the electrode, washed with dimethyl carbonate, then the morphology and composition were examined with SEM and EDX mapping and the results were compared with previously untested samples (Fig. 5a). The color maps revealed the homogeneous distribution of Ni, Fe and S throughout the entire particles of C, Mo, and Se nanosheets. Furthermore, even after 4000-cycle of testing, the SEM and EDX mapping of Ni_{1+x}-Fe$_{2-x}$S$_4$-g-MoSe$_2$ appeared essentially identical to the original samples (Fig. 5b). This suggested that the morphology and composition of the $Ni_{1+x}Fe_{2-x}S_4$-g-MoSe$_2$ nanocomposites underwent no change during cycling. By contrast, the SEM and EDX mappings of $Ni_{1+x}Fe_{2-x}S_4$-g before and after cycle tests varied greatly (Fig. 6).

Based on the experimental results, the unique performance of $Ni_{1+x}Fe_{2-x}S_4$-g-MoSe$_2$ nanocomposite could be explained by the following mechanism: first, the graphene sheets significantly facilitated the electron transport during the charge and discharge processes due to their high conductivities. This was confirmed by the EIS results shown in Fig. 7a. Also, they accelerated the ion diffusion demonstrated by the converted UV-Vis absorption spectra in Fig. 7b. Secondly, MoSe$_2$ served as a mechanical buffer to alleviate the volume change during the charge and discharge processes. Also, $Ni_{1+x}Fe_{2-x}S_4$ nanoparticles were strongly anchored into the graphene nanosheets because of their stable structures. Furthermore, the Ni_{1+x}-Fe$_{2-x}$S$_4$ particles acted as a spacer, preventing the graphene and MoSe$_2$ nanosheets from agglomerations. Thirdly, it is well-

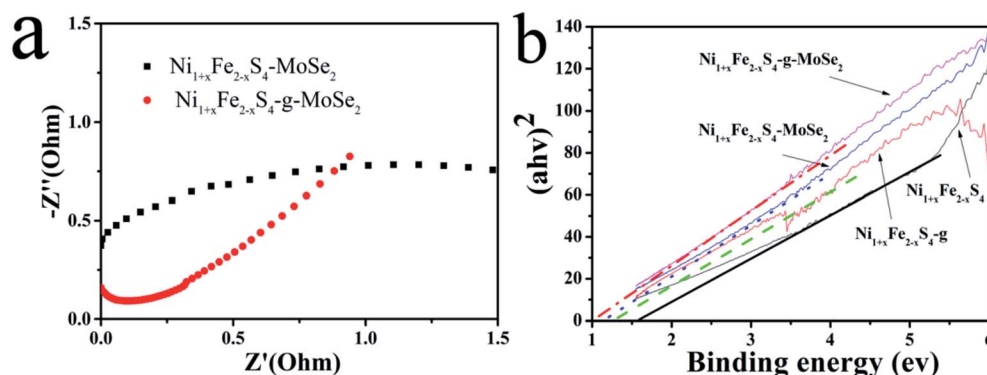**Fig. 7** (a) EIS curves of $Ni_{1+x}Fe_{2-x}S_4$-MoSe$_2$ and $Ni_{1+x}Fe_{2-x}S_4$-g-MoSe$_2$ and (b) DRS curves of $Ni_{1+x}Fe_{2-x}S_4$, $Ni_{1+x}Fe_{2-x}S_4$-g, $Ni_{1+x}Fe_{2-x}S_4$-MoSe$_2$, and $Ni_{1+x}Fe_{2-x}S_4$-g-MoSe$_2$.

known that a higher specific surface areas and larger pore volumes of composites are beneficial for enhancing the photocatalytic performance. The N_2 adsorption–desorption isotherm of $Ni_{1+x}Fe_{2-x}S_4$, $Ni_{1+x}Fe_{2-x}S_4$-g and $Ni_{1+x}Fe_{2-x}S_4$-g-$MoSe_2$ are shown in Fig. S6,† the specific surface areas of $Ni_{1+x}Fe_{2-x}S_4$, $Ni_{1+x}Fe_{2-x}S_4$-g and $Ni_{1+x}Fe_{2-x}S_4$-g-$MoSe_2$ are 9.5, 34.5 and 49.2 $m^2\ g^{-1}$, respectively. Finally, the synergistic effect due to the three components in $Ni_{1+x}Fe_{2-x}S_4$-g-$MoSe_2$ resulted in enhanced electrochemical properties, where graphene provided fast ion/electron transfer, $Ni_{1+x}Fe_{2-x}S_4$ boosted the supercapacity of the nanocomposite, and $MoSe_2$ improved the cycling stability.

5. Conclusions

Ternary $Ni_{1+x}Fe_{2-x}S_4$-g-$MoSe_2$ was prepared for the first time through a two-step hydrothermal method followed by *in situ* absorption. The resulting microstructures consisted of well-dispersed $MoSe_2$ and graphene nanosheets connected with $Ni_{1+x}Fe_{2-x}S_4$ nanoparticles. The obtained $Ni_{1+x}Fe_{2-x}S_4$-g-$MoSe_2$ demonstrated superior electrochemical performances attributed to the synergistic effect between the 2D $MoSe_2$, highly conductive graphene networks, $Ni_{1+x}Fe_{2-x}S_4$ nanoparticles, and the stable three-dimensional architecture supporting each component. Thus, the sheet-sphere-sheet nanostructure was extremely stable during long-life charge–discharge processes, resulting in improved rate capability and cycling stability. The evaluation of $Ni_{1+x}Fe_{2-x}S_4$-g-$MoSe_2$ as electrode active material for SC revealed high specific capacitance and excellent cyclic stability. Moreover, the constructed electrodes from this material exhibited rapid electron and ion transport rates, with large electroactive surface areas. These findings indicated $Ni_{1+x}Fe_{2-x}S_4$-g-$MoSe_2$ as a promising electrode material for SC applications.

Conflicts of interest

There are no conflicts to declare.

References

1 D. Cai, D. Wang, B. Liu, Y. Wang, Y. Liu, L. Wang, H. Li, H. Huang, Q. Li and T. Wang, *ACS Appl. Mater. Interfaces*, 2013, **5**, 12905–12910.

2 P. Xiong, H. Huang and X. Wang, *J. Power Sources*, 2014, **245**, 937–946.

3 Z.-L. Wang, X.-J. He, S.-H. Ye, Y.-X. Tong and G.-R. Li, *ACS Appl. Mater. Interfaces*, 2014, **6**, 642–647.

4 Y. Zhao, L. Zhan, J. Tian, S. Nie and Z. Ning, *Electrochim. Acta*, 2011, **56**, 1967–1972.

5 B. D. Boruah and A. Misra, *ACS Energy Lett.*, 2017, **2**, 1720–1728.

6 X. Li, H. Xue and H. Pang, *Nanoscale*, 2017, **9**, 216–222.

7 X. Chia, A. Ambrosi, Z. Sofer, J. Luxa and M. Pumera, *ACS Nano*, 2015, **9**, 5164–5179.

8 S. Peng, L. Li, H. B. Wu, S. Madhavi and X. W. Lou, *Adv. Energy Mater.*, 2015, **5**, 1401172.

9 L. Cao, S. Yang, W. Gao, Z. Liu, Y. Gong, L. Ma, G. Shi, S. Lei, Y. Zhang, S. Zhang, R. Vajtai and P. M. Ajayan, *Small*, 2013, **9**, 2905–2910.

10 W. Cai, T. Lai, W. Dai and J. Ye, *J. Power Sources*, 2014, **255**, 170–178.

11 B. D. Boruah and A. Misra, *J. Mater. Chem. A*, 2016, **4**, 17552–17559.

12 B. Li, P. Gu, Y. Feng, G. Zhang, K. Huang, H. Xue and H. Pang, *Adv. Funct. Mater.*, 2017, **27**, 1605784.

13 X. Wang, B. Liu, R. Liu, Q. Wang, X. Hou, D. Chen, R. Wang and G. Shen, *Angew. Chem., Int. Ed.*, 2014, **53**, 1849–1853.

14 Y. Chen, B. Liu, Q. Liu, J. Wang, J. Liu, H. Zhang, S. Hu and X. Jing, *Electrochim. Acta*, 2015, **178**, 429–438.

15 X. Li, S. Ding, X. Xiao, J. Shao, J. Wei, H. Pang and Y. Yu, *J. Mater. Chem. A*, 2017, **5**, 12774–12781.

16 H. Pang, X. Li, Q. Zhao, H. Xue, W.-Y. Lai, Z. Hu and W. Huang, *Nano Energy*, 2017, **35**, 138–145.

17 S. Chen and S.-Z. Qiao, *ACS Nano*, 2013, **7**, 10190–10196.

18 H. Jiang, Y. Dai, Y. Hu, W. Chen and C. Li, *ACS Sustainable Chem. Eng.*, 2014, **2**, 70–74.

19 Y. Xu, G. Shi and X. Duan, *Acc. Chem. Res.*, 2015, **48**, 1666–1675.

20 M.-C. Liu, L.-B. Kong, C. Lu, X.-J. Ma, X.-M. Li, Y.-C. Luo and L. Kang, *J. Mater. Chem. A*, 2013, **1**, 1380–1387.

21 L.-Q. Mai, F. Yang, Y.-L. Zhao, X. Xu, L. Xu and Y.-Z. Luo, *Nat. Commun.*, 2011, **2**, 381.

22 L. Huang, D. Chen, Y. Ding, Z. L. Wang, Z. Zeng and M. Liu, *ACS Appl. Mater. Interfaces*, 2013, **5**, 11159–11162.

23 Y. Song, T.-Y. Liu, X.-X. Xu, D.-Y. Feng, Y. Li and X.-X. Liu, *Adv. Funct. Mater.*, 2015, **25**, 4626–4632.

24 G. Ćirić-Marjanović, *Synth. Met.*, 2013, **170**, 31–56.

25 H. Ben, M. Julian, W. Shuang, I. Jung Bin, C. Carlo, P. Dimos, P. G. Costas and M. Roya, *Nanotechnology*, 2014, **25**, 055401.

26 G. Nystrom, A. Marais, E. Karabulut, L. Wagberg, Y. Cui and M. M. Hamedi, *Nat. Commun.*, 2015, **6**, 7259.

27 E. G. da Silveira Firmiano, A. C. Rabelo, C. J. Dalmaschio, A. N. Pinheiro, E. C. Pereira, W. H. Schreiner and E. R. Leite, *Adv. Energy Mater.*, 2014, **4**, 175–178.

28 H. Hu, K. Zhang, S. Li, S. Ji and C. Ye, *J. Mater. Chem. A*, 2014, **2**, 20916–20922.

29 S. Peng, L. Li, C. Li, H. Tan, R. Cai, H. Yu, S. Mhaisalkar, M. Srinivasan, S. Ramakrishna and Q. Yan, *Chem. Commun.*, 2013, **49**, 10178–10180.

30 D. Guo, P. Zhang, H. Zhang, X. Yu, J. Zhu, Q. Li and T. Wang, *J. Mater. Chem. A*, 2013, **1**, 9024–9027.

31 Y. Zhang, W. Sun, X. Rui, B. Li, H. T. Tan, G. Guo, S. Madhavi, Y. Zong and Q. Yan, *Small*, 2015, **11**, 3694–3702.

32 L. Niu, Z. Li, Y. Xu, J. Sun, W. Hong, X. Liu, J. Wang and S. Yang, *ACS Appl. Mater. Interfaces*, 2013, **5**, 8044–8052.

33 M.-C. Liu, L.-B. Kong, C. Lu, X.-M. Li, Y.-C. Luo and L. Kang, *ACS Appl. Mater. Interfaces*, 2012, **4**, 4631–4636.

34 G. Wang, Q. Tang, H. Bao, X. Li and G. Wang, *J. Power Sources*, 2013, **241**, 231–238.

35 K.-J. Huang, L. Wang, Y.-J. Liu, H.-B. Wang, Y.-M. Liu and L.-L. Wang, *Electrochim. Acta*, 2013, **109**, 587–594.

36 R. B. Rakhi, W. Chen, D. Cha and H. N. Alshareef, *Adv. Energy Mater.*, 2012, **2**, 381–389.

37 J.-G. Wang, Y. Yang, Z.-H. Huang and F. Kang, *J. Mater. Chem.*, 2012, **22**, 16943–16949.

38 N. Kurra, C. Xia, M. N. Hedhili and H. N. Alshareef, *Chem. Commun.*, 2015, **51**, 10494–10497.

39 X. Zhang, Z. Lin, B. Chen, W. Zhang, S. Sharma, W. Gu and Y. Deng, *J. Power Sources*, 2014, **246**, 283–289.

40 X. Yu, B. Lu and Z. Xu, *Adv. Mater.*, 2014, **26**, 1044–1051.

41 M. S. Javed, S. Dai, M. Wang, D. Guo, L. Chen, X. Wang, C. Hu and Y. Xi, *J. Power Sources*, 2015, **285**, 63–69.

42 M. Acerce, D. Voiry and M. Chhowalla, *Nat. Nanotechnol.*, 2015, **10**, 313–318.

43 J. N. Coleman, M. Lotya, A. O'Neill, S. D. Bergin, P. J. King, U. Khan, K. Young, A. Gaucher, S. De, R. J. Smith, I. V. Shvets, S. K. Arora, G. Stanton, H.-Y. Kim, K. Lee, G. T. Kim, G. S. Duesberg, T. Hallam, J. J. Boland, J. J. Wang, J. F. Donegan, J. C. Grunlan, G. Moriarty, A. Shmeliov, R. J. Nicholls, J. M. Perkins, E. M. Grieveson, K. Theuwissen, D. W. McComb, P. D. Nellist and V. Nicolosi, *Science*, 2011, **331**, 568–571.

44 P. Hu, T. Chen, Y. Yang, H. Wang, Z. Luo, J. Yang, H. Fu and L. Guo, *Nanoscale*, 2017, **9**, 1423–1427.

45 B. D. Boruah, A. Maji and A. Misra, *Nanoscale*, 2017, **9**, 9411–9420.

46 S. K. Balasingam, J. S. Lee and Y. Jun, *Dalton Trans.*, 2015, **44**, 15491–15498.

47 V. Nicolosi, M. Chhowalla, M. G. Kanatzidis, M. S. Strano and J. N. Coleman, *Science*, 2013, **340**, 6139.

48 T. Heine, *Acc. Chem. Res.*, 2015, **48**, 65–72.

49 X. Tang, Z. Yang and J. Liang, *RSC Adv.*, 2016, **6**, 88168–88173.